The Cryosphere

Open Access

EGU

Supraglacial lake bathymetry automatically derived from ICESat-2 constraining lake depth estimates from multi-source satellite imagery

Rajashree Tri Datta[1,2,3,★] **and Bert Wouters**[4,5,★]

[1]Earth Systems Science Interdisciplinary Center, University of Maryland, College Park, MD, USA
[2]NASA Goddard Space Flight Center, Greenbelt, MD, USA
[3]Department of Atmospheric and Oceanic Sciences, University of Colorado Boulder, Boulder, CO, USA
[4]Institute for Marine and Atmospheric Research, Department of Physics, Utrecht University, Utrecht, the Netherlands
[5]Faculty of Civil Engineering and Geosciences, Delft University of Technology, Delft, the Netherlands
[★]These authors contributed equally to this work.

Correspondence: Rajashree Tri Datta (tri.datta@gmail.com)

Abstract. We introduce an algorithm (Watta) which automatically calculates supraglacial lake bathymetry and detects potential ice layers along tracks of the ICESat-2 (Ice, Cloud, and Land Elevation Satellite) laser altimeter. Watta uses photon heights estimated by the ICESat-2 ATL03 product and extracts supraglacial lake surface, bottom, and depth corrected for refraction and (sub-)surface ice cover in addition to producing surface heights at the native resolution of the ATL03 photon cloud. These measurements are used to constrain empirical estimates of lake depth from satellite imagery, which were thus far dependent on sparse sets of in situ measurements for calibration. Imagery sources include Landsat 8 Operational Land Imager (OLI), Sentinel-2, and high-resolution Planet Labs PlanetScope and SkySat data, used here for the first time to calculate supraglacial lake depths. The Watta algorithm was developed and tested using a set of 46 lakes near Sermeq Kujalleq (Jakobshavn) glacier in western Greenland, and we use multiple imagery sources (available for 45 of these lakes) to assess the use of the red vs. green band to extrapolate depths along a profile to full lake volumes. We use Watta-derived estimates in conjunction with high-resolution imagery from both satellite-based sources (tasked over the season) and nearly simultaneous Operation IceBridge CAMBOT (Continuous Airborne Mapping By Optical Translator) imagery (on a single airborne flight) for a focused study of the drainage of a single lake over the 2019 melt season. Our results suggest that the use of multiple imagery sources (both publicly available and commercial), in combination with altimetry-based depths, can move towards capturing the evolution of supraglacial hydrology at improved spatial and temporal scales.

1 Introduction

Ice loss from Greenland and Antarctica is the greatest current contributor to rising sea levels, and paleodata and modeling efforts indicate that enhanced mass loss of these ice sheets may become irreversible if certain major tipping points are passed (IPCC, 2019). Recent observations have shown that ice loss is accelerating faster than projected (Slater et al., 2020), with a sixfold increase since the 1970s and 1980s. In Antarctica, this was largely driven by increased ocean melting of outlet glaciers (Rignot et al., 2019), while on the Greenland Ice Sheet mass loss is further promoted by increased surface melt and runoff (Mouginot et al., 2019).

Owing to the nonlinear relationship between increasing summer air temperatures and surface melt (Trusel et al., 2018), meltwater production has increased rapidly on the Greenland Ice Sheet (van den Broeke et al., 2016). In the summer of 2019, advection of warm, wet mid-latitude air led to a summer mass loss unprecedented in the past 50 years,

with widespread surface melt occurring up to the highest regions of the ice sheet (Tedesco and Fettweis, 2020; Sasgen et al., 2020). Concurrent with the increase in melt extent and duration, supraglacial lakes – which form when meltwater runoff collects in local topographic lows – are now a common feature on large parts of the ice sheets and have become more extensive and have advanced inland toward higher elevations in the past decades (Gledhill and Williamson, 2018; Leeson et al., 2015; Howat et al., 2013).

These meltwater lakes and streams are a key component of the hydrological system of both ice sheets. Hydrological systems over Antarctic ice shelves have been identified as a major factor for potential ice shelf collapse (Bell et al., 2018). While mass loss in Antarctica over the next 100 years is generally thought to be dominated by the basal melt under ice shelves (Schlegel et al., 2018), emerging research has focused on the potential importance of surface hydrology over Antarctica (Arthur et al., 2020). Supraglacial lakes have been observed around the margin of the Antarctic Ice Sheet up to high elevations (Stokes et al., 2019) and are likely to become more prevalent on firn-depleted ice shelves in future warming scenarios, which could potentially trigger their collapse and consequently lead to accelerated sea level rise (Lai et al., 2020). Meltwater pathways can include surface flow into lakes and then streams, leading, in Greenland, to direct loss to the bed from lake drainage or the sudden termination of a stream into a moulin, or near-surface flow in which ice slabs can limit vertical motion (MacFerrin et al., 2019). The complex links between supraglacial hydrological systems and englacial or subglacial pathways can potentially be deduced by capitalizing on increasingly higher-resolution imagery and classification techniques of supraglacial feature types (Yang et al., 2017). Past remote-sensing work has derived lake volumes from high-resolution ($\sim$ 1 m) WorldView imagery using a physical optical depth approach, as well as an empirical method using in situ estimates (Moussavi et al., 2016; Pope et al., 2016). Recent work has developed an automated algorithm applying the physically based method to Landsat 8 and Sentinel 2 to track specific hydrological features and quantify the seasonal evolution of surface hydrology (Dell et al., 2020). The physical method assumes that wind-driven surface waves are minimal, that the slope of lake bottoms are gradual, and that lake-bottom albedos are homogeneous (Sneed and Hamilton, 2011). The empirically based method was first applied by Box and Ski (2007) using MODIS imagery and advanced by Legleiter et al. (2014), who used high-resolution WorldView 2 imagery. Both the physically based and empirically based methods are limited to supraglacial lakes which contain minimal particulate matter (Arthur et al., 2020) and by the depth of the lake, assuming that the reflection depletion in imagery is limited at great depths, implying a physical limit to the ability to calculate depth (Box and Ski, 2007). Pope et al. (2016) estimate that the greatest depth that could be calculated by these methods was 5 m. Additional work has applied a sim-

ilar physically based approach using Sentinel-2 from Copernicus (Williamson et al., 2018), Landsat 7 and 8 (Banwell et al., 2014), Aster imagery (Sneed and Hamilton, 2007), and a combination of Landsat and Sentinel-2 imagery (Moussavi et al., 2020). Although Sentinel-2 provides relatively high-resolution (10 m) imagery with substantial coverage at a 4 d to weekly interval, usable imagery is often limited by cloud-cover, and the resolution of small streams and ice cover is imperfect. Commercial satellite imagery, which is poised to expand substantially in the future, can help fill the gap in coverage of small-scale melt and melt-induced features at a higher spatial (< 3 m) and temporal (multiple daily passes) resolution, complementing estimates resolved from Sentinel-2.

The ICESat-2 (Ice, Cloud, and Land Elevation Satellite) laser altimeter data, available since 2018, has now introduced the potential to replace the in situ measurements used in empirical (supraglacial lake depth) bathymetric methods with satellite laser bathymetric depths at a high vertical resolution, consequently extracting lake volumes from imagery (Parrish et al., 2019; Albright and Glennie, 2020; Thomas et al., 2021). Here, we present a new algorithm, titled "Watta", using the ICESat-2 laser altimeter to derive properties of supraglacial lakes. Watta was first presented in Fricker et al. (2020), demonstrating both the potential for ICESat-2-based bathymetry estimates and the greater accuracy of empirically based lake depths in comparison to physically based estimates; the latter tended to underestimate lake depth by over 2 m. However, we note that physically based methods have the advantage of being dependent on imagery alone. In addition to bathymetry derived from the difference between the air–water and water–ice interface, this algorithm assigns a probability for surface type characteristics to photon returns along track. These types include lakes, refrozen lakes, and lakes with ice layers on top and under the surface. Watta also returns surface heights at the native resolution of the ATL03 photon cloud (0.7 m), allowing the algorithm to capture small-scale changes in surface relief when multiple passes are differenced. Additionally, we exploit a range of imagery data to validate the surface types and to derive spectrally driven depth estimates calibrated to ICESat-2-based depths, thereby providing an estimate for meltwater volume over the full image. We compare empirically based volume estimates derived from a single ICESat-2-based depth estimate but from multiple imagery sources with different spatial resolutions (and without an atmospheric correction) to better understand the importance of spatial resolution and radiometric calibration for the relative accuracy of depth volume estimates.

The method is tested and refined using representative sections along the flowline of Sermeq Kujalleq (Jakobshavn Isbræ), one of the fastest-moving glaciers in Greenland, as well as the slower-flowing Sarqardliup Sermia. The repeat tasking of Planet SkySat imagery was designed to coincide with ICESat-2 tracks (Fig. 1), capturing lake depths at var-
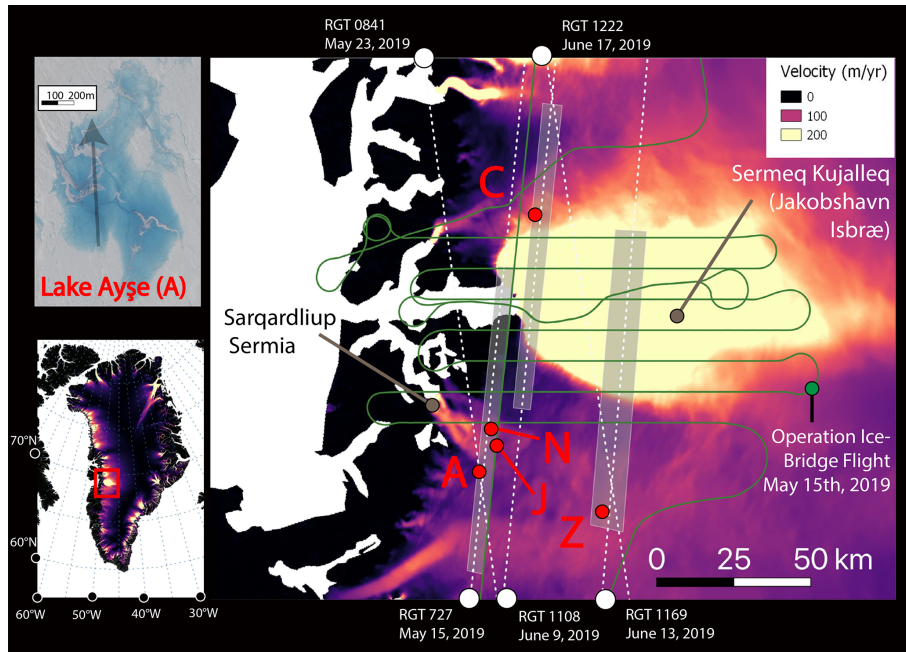
Figure 1. Study region over Sermeq Kujalleq and Sarqardliup Sermia. Top left panel: Lake Ayşe on 23 May using Planet SkySat Visual imagery. Bottom left panel: study region over western Greenland. Right panel: main region with repeat-tasking locations for Planet SkySat shown in grey boxes over annual velocity estimates from MEaSUREs (NSIDC). ICESat-2 reference ground tracks shown in white. Operation IceBridge flight on 15 May 2019 shown in green. Five lakes indicated in red discussed throughout text include the following: C: Lake Cecily; A: Lake Ayşe; J: Lake Julian; N: Lake Niels; Z: Lake Zadie.

ious stages of lake development during the unusually intense melt season of summer of 2019 (Tedesco and Fettweis, 2020). One of the major motivations for this tasking effort was its coincidence with several NASA Operation IceBridge (OIB) flights at the beginning and end of the summer. Data from multiple instruments on board OIB could potentially provide additional insight in future work, and within this study, we use OIB CAMBOT (Continuous Airborne Mapping by Optical Translator) imagery as a part of a focused multi-instrument study of the evolution of a supraglacial lake. The availability of simultaneous laser altimetry and high-resolution imagery over the season provided a rich test dataset with which to extract altimetry-based estimates of supraglacial lakes at various points in the season. Here, we present initial results exploiting this dataset, as well as introducing the Watta ICESat-2 surface feature detection algorithm.

2 Data sources

2.1 Satellite altimetry

Our Watta method relies on individual photon heights as measured by ICESat-2's (Ice, Cloud, and Land Elevation Satellite) ATLAS (Advanced Topographic Laser Altimeter System) instrument, distributed in the ICESat-2 ATL03 prod-

uct, L2A, Global Geolocated Photon Data (Neumann et al., 2019). The polar orbiting ICESat-2 satellite was launched in September 2018 to continue the mission begun by ICESat (2003–2009) and bridged with the airborne Operation IceBridge mission, namely to provide ice sheet mass balance estimates at an unprecedented level of accuracy. ATLAS is a photon-counting 532 nm laser altimeter on board ICESat-2 split into six beams which are divided into three pairs (separated by 3.3 km), in which beams within each pair are separated by 90 m. Within a single track, the beam pair is designated by a number, e.g., "3" in "gt3r". Each beam pair consists of a strong and weak beam, with the strong beam returning 0.6–3.9 signal photons per laser pulse vs. 0.6–1.0 signal photons per laser pulse for the weak beam (Neumann et al., 2019). The beam is designated with "r" or "l" depending on the orientation of the satellite, as in "r" in "gt3r".

While the strong beam produces a stronger signal, we have developed the Watta algorithm to work effectively with both strong and weak beams. ATL03 produces a photon cloud in which each photon is geolocated to within a 6.5 m accuracy and a footprint size of ~ 11 m (Magruder et al., 2021) with an associated height, as well as a confidence level (high, medium, or low), and is produced at an along-track horizontal resolution of 0.7 m. While the ATL06 product (Smith et al., 2019) provides highly accurate surface height estimates at a coarser resolution, the higher spatial resolution of the ATL03 product can be used to deduce fine-scale surface char-

acteristics, as with the Watta algorithm. Over water bodies, ICESat-2 can produce returns both over the surface and over the lake, as well as the bottom of the lake (Fair et al., 2020; Fricker et al., 2020; Parrish et al., 2019); these dual returns are used by Watta to extract supraglacial lake depths, as well as lake surface characteristics.

2.2 High-resolution imagery near Sermeq Kujalleq

For imagery sources, in addition to freely available Landsat Operational Land Imager (OLI; 30 m) and Sentinel-2 (10 m) imagery, we incorporate very high-resolution imagery from Planet Labs, including Dove-R (3 m) and SkySat ($\sim$ 1 m). The latter is used to validate surface types, while all imagery sources are used to derive spectrally driven depth estimates calibrated to ICESat-2-based depths. Additionally, the high spatial resolution of SkySat imagery allows for the identification of small-scale features on the surface and bottom of supraglacial lakes, which we use to interpret the temporal evolution of lake characteristics in a number of case studies. SkySat imagery did not include an atmospheric correction, and we therefore used TOA (top of the atmosphere) reflectance values from Landsat, Sentinel-2, and SkySat imagery to calculate supraglacial lake depth for the sake of consistency. PlanetScope Dove-R data provided surface reflectance values only and are known to have issues with radiometry (Saunier, 2020). However, because the method used here derives lake depth values empirically (rather than physically), this work presents the opportunity to develop accurate depth estimates using high-resolution data for which calibration is imperfect but the data availability is high. This is particularly true for data from the PlanetScope constellation, which are frequently captured multiple times within a single day. Relative spectral response curves for the bands used in this study are red, blue, green, and near infrared (NIR), as shown in Fig. S1b in the Supplement. Finally, all imagery was coregistered with ICESat-2 using the GIMP-2 digital elevation model (DEM), which has a vertical accuracy (as compared to ICESat) within ±1 m over most ice surfaces and ±30 m over areas with high relief (Howat et al., 2014) and is used for the geolocation of Landsat imagery (detailed in Sect. 3.2).

As a part of this project, SkySat imagery was tasked for repeat cycles of $\sim$ 4 d over the 2019 Greenland melt season in selected locations, producing usable imagery at varying intervals based on cloud cover. Each of the three areas of interest presented here were approximately 600 km^2. Repeat imagery was specifically chosen to cover flowlines of fast-flowing glaciers, including Sermeq Kujalleq, as in this study (Fig. 1). In addition, repeat tracks were designed to coincide with both (a) overpasses of the recently launched NASA ICESat-2 laser altimeter and (b) several flights of the airborne NASA Operation IceBridge (OIB) mission in the beginning and end of the season. Here, we present the first work exploiting this stacked dataset for method development, restricted

to available satellite imagery and altimetry. We note that for Lake Julian, discussed in Sect. 5, OIB conducted a flight on 15 May 2019, thus capturing observations from multiple instruments onboard OIB, including CAMBOT imagery and the Airborne Topographic Mapper (ATM). While ATM-based lake depth estimates could potentially be compared to the lake depths calculated from the near-simultaneous ICESat-2 overpass, this is outside the scope of this study. We discuss Lake Julian in detail in order to facilitate potential future research at this site.

The final set of lakes used for the development of the Watta method included 50 lakes captured by ICESat-2 (46 over Sermeq Kujalleq and Sarqardliup Sermia and 4 additional lakes in the southwest, not shown here), 14 of which coincided with very high-resolution imagery (SkySat) within a 3 d window. The date, time, and imagery IDs and ICESat-2 details for all data sources are presented in Table S1 in the Supplement.
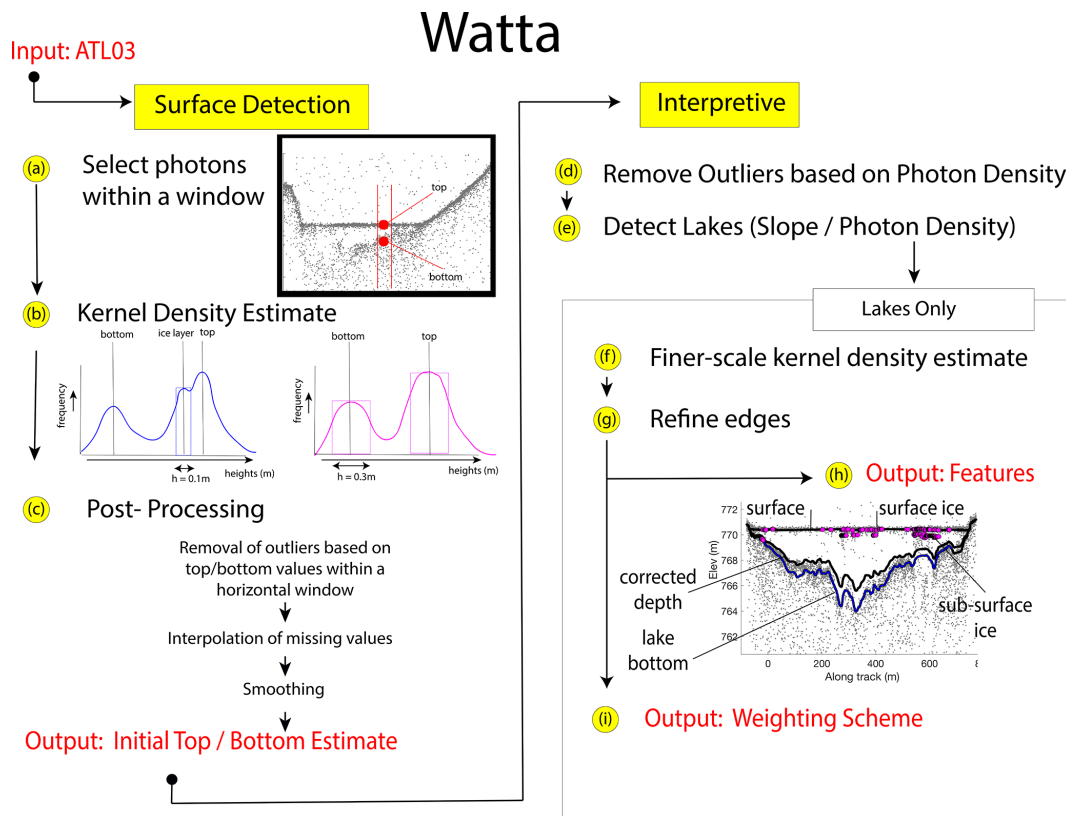
3 Methods

We derive supraglacial lake volume from a given imagery source in four steps. We first calculate lake depths along an ICESat-2 beam using the Watta algorithm applied to the ICESat-2 ATL03 photon cloud. Secondly, we coregister Watta-based surface and lake bottom heights with the imagery source (itself coregistered to a common Landsat base) and delineate lake boundaries in the process (methods detailed in Sect. 3.2). Finally, we develop an empirical relationship between ICESat-2-based depths and coincident imagery which can be applied to calculate lake depths over the full image. The empirical relationship is based on the exponential decay of reflectance at water depth, as detailed by Box and Ski (2007). In the original work, in situ depth estimates (D) and reflectance values from imagery (R) were used to estimate the α coefficients in Eq. (1), which were then applied to calculate water depth over the full scale of imagery where lakes are delineated:

$$D = \alpha_0 / (R + \alpha_1) + \alpha_2. \tag{1}$$

However, such in situ estimates are scarce in space and time, and here we exploit the direct depths from the Watta algorithm to derive time, location, and sensor-specific estimates of the α coefficients.

3.1 Watta

Watta is an algorithm which takes ICESat-2 ATL03 photon data as input and automatically detects supraglacial surface features with an associated likelihood. In its current state, the algorithm detects lakes and their associated surface, lake bottom, and corrected depth estimates, as well as subsurface ice when present (Fig. 2). We also exploit the algorithm for the detection of frozen streams in this study. The

Figure 2. Diagram of the Watta methods described in main text.

codebase for Watta is divided into a module which calculates surface and bottom returns ("Surface Detection") at the native 0.7 m resolution of ICESat-2 and a second "Interpretive" module that resolves the calculated bottom and surface to specific supraglacial features, in this case lakes. The Surface Detection module determines, for a collection of photons surrounding any individual photon (75 collected before and 75 collected after; selected in step a), heights with the three strongest peak probabilities within a kernel density (step b). This provides estimates for (1) a height for the surface or top of a lake or refrozen pond, (2) a lake bottom, and (3) a third height value, which can potentially be subsurface ice (Fig. 2, step a). We note that photons are selected without regard to ATL03 confidence level. Although the bin width (and therefore vertical resolution) used to calculate heights is 0.1 m, we perform a second kernel density estimate calculation using a 0.3 m bin width to confirm robustness of the initial bottom estimate, i.e., that a coarser calculation produces a bottom height near that of the finer-resolution (0.1 m bin width) calculation. In post-processing step c, outliers are identified in comparison to surface and bottom heights within a larger horizontal window, whereby the number of standard deviations used to detect an outlier and the number of photons used to calculate a mean (window) increase over several steps. Where outliers are found, the kernel density estimate

(steps a and b) are recalculated with a larger number of photons (in multiples of 75) to account for any erroneous calculations generated by insufficient photon density. Where values continue to be outliers, they are removed from the estimates to be interpolated instead. The final output of the Surface Detection module includes a calculated surface and potential lake bottom return at the native resolution of the ATL03 photon cloud.

The Interpretive module uses output from the Surface Detection module to automatically determine locations of surface features (e.g., lakes or frozen streams), as well as characteristics of a lake, e.g., the presence of refrozen ice at the surface. First, remaining outliers are removed by calculating a local background and surface photon density for each ATL03 photon, as determined from a 5000 photon-count window surrounding the estimate location (step d). We then remove those estimated heights for top (surface) and bottom (potential lake bottom) where the photon density more closely resembles the background photon density than a surface density estimate. In step e, we detect breaks in the slope of the top (surface) to divide the satellite pass into segments which are potential lakes. For example, a semi-parabolic depression in topography, with a high absolute value of the slope, is broken by a lake surface where the slope approaches zero (e.g., as for the lake shown in Fig. 2, step a). For each of

Imagery Processing
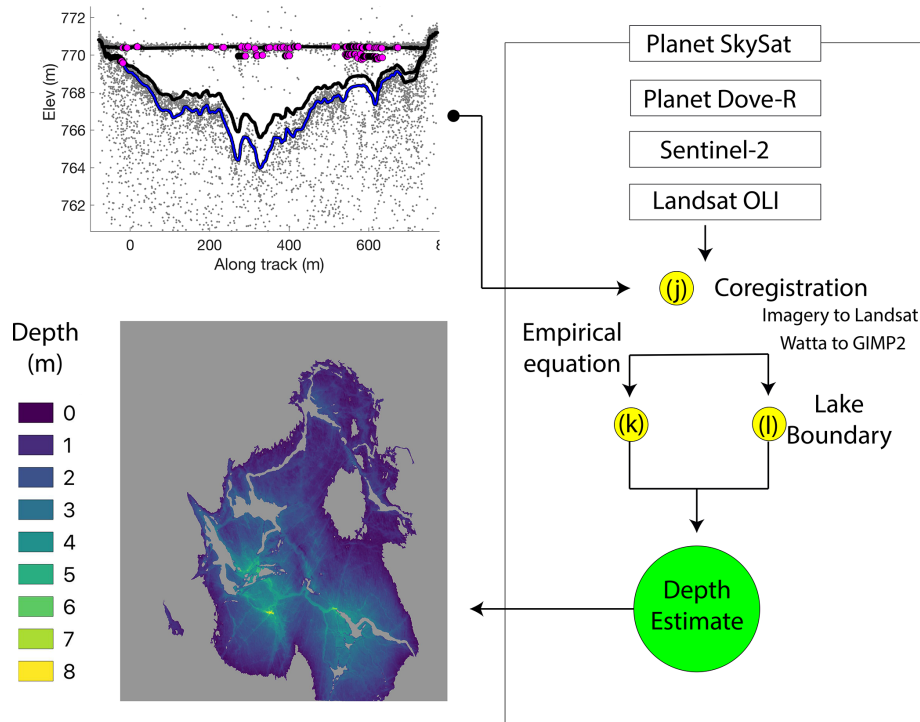
Figure 3. Diagram of imagery processing steps accepting Watta outputs as input (top left panel) and producing lake depth estimates (bottom left panel). The Watta lake depth profile shown is for Lake Ayşe using RGT 841 on 23 May and Planet SkySat imagery on 22 May.

these potential lakes, we then perform several steps both to refine lake surface and bottom and to assign the lake a class based on its properties. To produce a lake bottom value with greater accuracy, we first perform a recalculation of the kernel density estimate (step f, equivalent to the Surface Detection step b), except here we limit the kernel density estimate to photons below the calculated surface and use 30 photons rather than 75 photons to better capture the lake bathymetry, which in general is more irregular than the lake surface. Subsurface ice layers near the edges of the lake are then reclassified as lake surfaces, thus sealing the bottom of the lake to the top at the lake edges (step g). In step h, we first perform a final smoothing, passing the resulting bottom photons through an iterative robust quadratic local regression (rloess) filter to remove outliers in the bottom estimates and then assign physical meaning to each photon (e.g., lake surface, bottom, surface ice, subsurface ice). The presence of surface ice is determined based on the variability in thickness of the lake surface (i.e., a bimodal distribution indicates surface ice at some locations). We identify subsurface ice by the presence of weak returns above the lake bottom but below the surface (see Fig. 2, step b). The surface and bottom photons are then used to derive lake depth, to which we apply a simple correction for refraction, described in Parrish et al. (2019), to

produce a real corrected lake depth. Finally, in step i, we assign a final classification of a lake type using properties of the local surface slope and the strength of the bottom return (Table 1). For example, a segment with a surface slope smaller than 0.03 %, as well as a distinct bottom (a photon density far exceeding the density of a background return), is given a lake classification of "highly likely", whereas segments passing the same slope threshold but not showing a strong bottom return are identified as "likely ice-covered" lakes. On the other hand, segments with a slope exceeding 0.3 % and no significant peak below the surface in the histogram are allocated to the "highly unlikely" lake class.

Two potential sources of ambiguity with the subsurface ice classification are (a) the possibility for specular returns and (b) apparent multiple surface returns which result from instrument echo. Specular returns over flat water (implying high energy return) return a strong surface, as well as multiple layers below the surface spaced according to the ATLAS dead time (0.45 m below the surface and a potential tertiary return below that). Echoes produced by electronic noise in the instrument, which also frequently occur on very smooth water surfaces, can similarly produce a strong return at the surface with double echoes at ~ 2.3 and ~ 4.2 m below the surface (Martino et al., 2020; Lu et al., 2021). The catego-

Table 1. Definitions for Watta lake classes.

Class	Slope	Bottom reflection*	Lake probability	Lake characteristics
1	$< 0.03\%$	Strong	Highly likely	Very flat open lake, dense bottom photon returns
2	$0.3\% < \text{slope} < 0.3\%$	Strong	Very likely	Flat, open lake with presence of refrozen ice; dense bottom photon returns
3	$> 0.3\%$	Strong	Likely	Non-flat surface, possibly flowing water channel on sloping surface; dense bottom photon returns
4	$< 0.03\%$	Weak	Very likely	Very flat open lake; weak bottom photon returns
5	$0.3\% < \text{slope} < 0.3\%$	Weak	About as likely as not	Flat open lake; weak bottom photon returns
6	$> 0.3\%$	Weak	Unlikely	Non-flat surface; weak bottom photon returns
7	$< 0.03\%$	None	Likely	Very flat refrozen lake; no significant bottom photon returns

* Strength of the bottom reflection is defined by the ratio of the first two peaks in the 2 m interval histogram of non-surface photon heights within the segment. Strong bottom reflection: peak ratio > 3.5; weak bottom reflection: 2.5 < peak ratio < 3.5; no bottom reflection: peak ratio < 0.

rization of subsurface ice (as with Lake Ayşe in Fig. 3) is reliant on visual inspection. In this case, we assume subsurface ice because the layer shows trailing photons towards a weakly resolved lake bottom rather than a distinctive sharp horizontal layer with no curved bottom return.

3.2 Imagery processing

A subsequent set of steps uses the lake depths extracted from the Watta algorithm to produce lake volumes from concurrent imagery, e.g., SkySat, PlanetScope, Sentinel-2, and Landsat OLI, requiring geolocation, as well as the semi-automated identification of lake edges. Coregistration between ICESat-2 photon locations and imagery (Fig. 3, step j) is managed by registering ICESat-2 elevations with the GIMP-2 DEM as an intermediary step (GIMP-2 is also used for georeferencing of Landsat) and by transforming the point cloud using the iterative closest point algorithm, which minimizes the square error between the two datasets (Besl and McKay, 1992). The point cloud ICESat-2 is chosen to include a 0.2° latitude window surrounding the lake resolved to include larger topography in the region (and thus avoid errors presented by ice motion). The large lakes used here are all located in strong topographic depressions (which are resolved in both the GIMP-2 DEM and ICESat-2) and can therefore be assumed to remain relatively fixed.

To register imagery sources to one another, we standardize all imagery to the nearest Landsat image using the arosics library in Python (Scheffler et al., 2017), which detects and corrects misregistrations of an input image (based on a reference image) at the sub-pixel scale. However, the coregistration of all other imagery sources to Landsat OLI first requires the delineation of lake boundaries in order to exclude regions with moving surface water, which evolves rapidly and can be mistaken for fixed topography (which is more useful for ge-

olocation). Here we calculated a normalized difference water index (NDWI) for each image, using a standard NDWI (with the green and NIR bands) to deliberately include regions with ice layers (as these are also detected by Watta) rather than the modified NDWI$_{ice}$ (which uses the red and blue bands) per Yang and Smith (2013). Boundaries of lakes (step l in Fig. 3) are calculated by using adaptive thresholding (Bradley and Roth, 2007) to generate a binary mask which is then used to identify individual water bodies. The use of adaptive thresholding avoids the limitations of any fixed NDWI threshold, especially relevant to PlanetScope data which occasionally produce negative NDWI values. However, we note that this step has the potential to include partial ice layers (although visual inspection suggests that this was avoided with the test cases used here). To coregister ICESat-2 to each imagery source, we also note that the ICESat-2 mission requirements list a geolocation accuracy of 6.5 m and a footprint size of ~ 11 m (Magruder et al., 2021), which may potentially include multiple pixels of high-resolution imagery. To calculate a band value from imagery associated with a geolocated photon from ICESat-2, we find pixels in imagery within a 6 m radius and calculate a mean. In Step k, we calculate an empirical relationship between the depth estimate calculated by Watta and a band value from coregistered imagery pixels. Finally, we use this empirical relationship to produce a depth estimate for the entire lake using Eq. (1).

4 Evaluating methodology

4.1 Physical constraints of the test dataset

The test dataset provides a diversity of lake types, with the largest surface area calculated at 5.6 km^2 and a maximum Watta-calculated corrected depth at 10.3 m. A number of

lakes contain substantial ice cover. In the following sections, we discuss several lakes in greater detail, which present a diverse set of conditions with which to evaluate both the Watta algorithm and the imagery sources used to extrapolate lake volumes. Locations of the lakes can be found in Fig. 1.

Lake Ayşe was selected for closer examination because, despite the dense photon cloud, its relief in surface and bottom, combined with the presence of ice cover, pose a challenge for our detection algorithm. Additionally, multiple imagery sources were available within a 5 d window at this location. Lake Zadie is chosen because it represents an ideal case for the algorithm, while Lake Cecily is chosen because two beams passed over the same lake with SkySat imagery available 1 d afterwards. A basic assumption we make in this study is that the lake bottom remains relatively consistent over several days, although past research on two lakes in western Greenland has estimated lake bottom ablation rates at $6.5\,\mathrm{cm\,d^{-1}}$ on the bottom of the pond (Tedesco et al., 2012). We assume that this is the primary physical source of uncertainty in the empirical calculation as the relationship will degrade with temporal distance from the ICESat-2 pass. However, where changes in the bathymetry are not uniform, we can potentially make inferences about drainage mechanisms (e.g., the forming and deepening of crevasses). Cross-sections of all lakes used for development showing the lake top, bottom, and bottom value corrected for refraction as calculated by Watta, along with lake top and bottom as calculated empirically from imagery, are shown in Fig. S4, and their coordinates and relevant statistics are listed in Table S1.

4.2 Physical constraints of the test dataset

The most rigorous weighting system used for the algorithm, using only lake classes 1, 2, 4, and 7 (see Table 1), succeeded in automatically detecting 49 out of the 50 lakes identified in the available imagery, with two likely false positives (i.e., not confirmed by NDWI values exceeding 0.2 in the imagery). A less rigorous weighting system, including lake class 3, detected the 50th lake but resulted in a large number of false positives in areas of steep and rough topography where abrupt changes in the photon elevations are misinterpreted as bottom reflections by the algorithm.

In the absence of simultaneous in situ data, we evaluate the performance of the algorithm based on visual inspection (comparing ATL03 heights with Watta-calculated depths as shown in Fig. S3). Additionally, where an empirical relationship with imagery is successful (a high correlation coefficient value between imagery-derived depths and Watta-derived depths), we take this consistency for partial evidence that ICESat-2 and imagery sources have detected bathymetry correctly, although we note that this metric is only applicable to the specific lake, not all the lakes in the region. The most successful bottom retrieval occurred where ice cover was minimal, the density of photons was high, and where the bottom slope was relatively uniform (e.g., Lake Zadie).

The presence of ice near the surface (between the surface and 1 m below the surface) frequently obscured lake bottom detection (e.g., reference ground track – RGT – 1222, Lake 3 in Fig. S3), although in some cases only partially; however, the presence of subsurface ice did not always preclude the presence of a strong bottom return (e.g., Lake 7, RGT 1169, Fig. S3). The algorithm therefore indicates the presence of surface and near-surface ice but does not automate the removal of the calculated bottom return due to ambiguity. We can confirm the presence of an ice layer both by visual inspection of the imagery and by comparing standardized NDWI values calculated from imagery coincident with the ICESat-2 track (Fig. S1a). We note that for at least one case (RGT 1108, Lake 6, Fig. S3), the designation of "lake" was ambiguous as this could be treated as either a shallow lake containing a large amount of subsurface ice or as a slush layer (a number of which were identified elsewhere).

4.3 Evaluating data sources for imagery-based depths

Total uncertainty for the empirically based depth estimates from imagery is comprised of uncertainty in ICESat-2 geolocation, uncertainty from the Watta algorithm itself (which operates at a vertical resolution of 0.1 m), from the resolution of the imagery, from the uncertainty in alpha coefficients calculated from the empirical method, and finally from physical changes in the lake occurring between the time that imagery is captured and the ICESat-2 pass. The empirical calculation is less likely to be affected by physical changes in the lake when the lake surfaces calculated by imagery vs. altimetry differ by less than a meter; here we estimate precision with a simple R^2 value.

Past work has considered either the red or green band for developing depth estimates (Moussavi et al., 2020; Williamson et al., 2018), though in situ validation was limited at the time (Pope et al., 2016). Figure 4 compares R^2 values from empirical estimates derived from the red vs. green band for lakes classified according to the maximum lake depth calculated by Watta. In agreement with Moussavi et al. (2016), for Landsat 8 (Fig. 4d), Sentinel-2 (Fig. 4c), and SkySat (Fig. 4a), the empirical depth estimates for the red band showed higher fidelity with Watta-based depths for shallow lakes, while the green band showed greater fidelity for deeper lakes. Of six lakes where a maximum depth exceeds 7.2 m and where the imagery source is Landsat 8, two lakes (RGT 1222, Lake 8, 12 in the Supplement profiles) show both red- and green-band-based profiles being unable to resolve the deepest points in the lake. For two additional cases (RGT 1222, Fig. 4e, Lake Zadie, Lake 14, 17 in the Supplement profiles), the green band was able to resolve very deep lake depths, while the red band was not. This implies that for SkySat, Sentinel-2, and Landsat 8, the green band is able to resolve bathymetry at greater depths and emphasize cracks at the bottom of the lakes. The major exception is PlanetScope data (Fig. 4b), in which the red band consis-
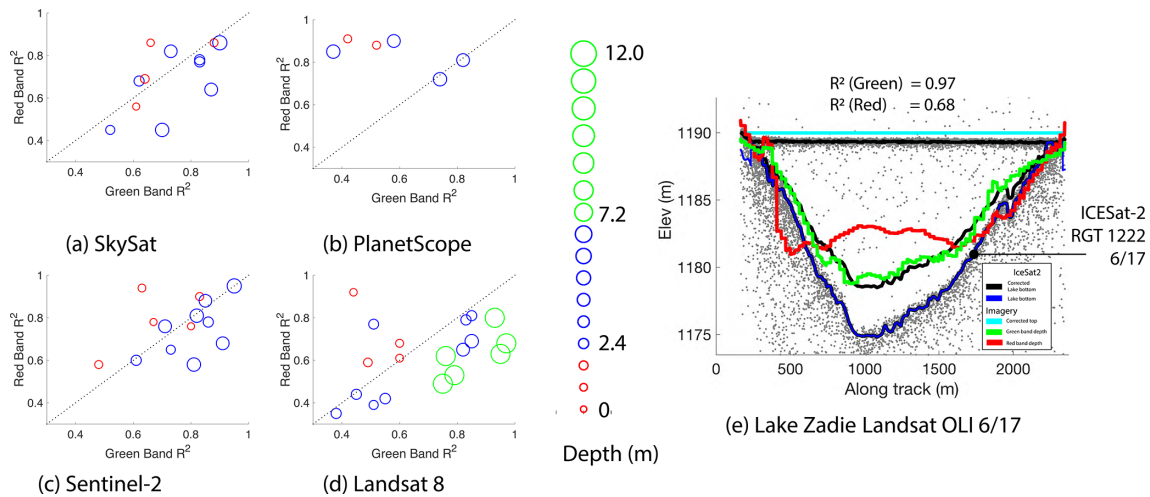
Figure 4. Comparing R^2 values from empirical estimates calculated with the red band vs. the green band from multiple imagery sources, with lakes classified by maximum lake depths as calculated by Watta. **(a)** Planet SkySat TOA reflectance. **(b)** Planet PlanetScope surface reflectance. **(c)** Sentinel-2 TOA reflectance. **(d)** Landsat 8 OLI TOA reflectance. **(e)** Watta-calculated and imagery-derived depths: Lake Zadie based on Landsat OLI.

tently showed greater fidelity to Watta-based estimates, while green band estimates produced unrealistic depth estimates, although there were a limited number of lakes where coincident PlanetScope imagery was available. We note that because this method is empirical, future users would be able to select bands or combinations, as with the average of the panchromatic and red band used by Pope et al. (2016).

To demonstrate the robustness of the Watta algorithm, the impact of band choice, and the sensitivity to absolute lake depth, we show depths calculated from two beams passing over Lake Cecily on 13 June, followed by retrieval of SkySat imagery on 14 June and Sentinel-2 on 16 June (Fig. 5a and b and RGT 1169 Lake 5, 6 in the Supplement profiles). Over this spot, covered by the 3l beam on this pass, the green band shows higher R^2 values for both Sentinel-2 and SkySat but lower R^2 values for the red band. This is consistent with the greater depths calculated from the 3l beam, which approach the 6 m depth where the performance of the green band is expected to improve. The use of the green band in both the 3l and 3r cases allows finer bathymetric relief to be captured in both SkySat- and Sentinel-based depth estimates, with the finer resolution of SkySat capturing substantially greater detail (Fig. 5c, box). We note that even when high R^2 values are calculated between the empirical estimate and Watta-calculated depths, unrealistic depths can result when lakes drain or fill rapidly, and low-resolution imagery can potentially resolve the height of a lake surface inaccurately (Fig. S2).

Within Fig. 6, we show the depth evolution of Lake Ayşe over 5 d, both along the ICESat-2 ATL03 and Watta-calculated profile and the lake volume estimates then constructed from imagery using the empirical equation. Increasing lake volume is demonstrated both by the expansion of the

surface area of the lake through time (right column) and the rise in the lake level (cyan line, left column). Planet SkySat estimates at a 1 m resolution (Fig. 6c) show the greatest level of detail of crevassing at the bottom of the lake although PlanetScope estimates at a 3 m resolution (Fig. 6d and e) are comparable. We note that PlanetScope data showed variations in the fidelity to Watta-based estimates between the green band vs. the red band depending on the instrument. The bottom relief is maintained at depth with the PlanetScope resolution (3 m), and future work could generate more reliable depth estimates by calibrating empirically based depths to Sentinel estimates, which could provide very high-resolution depth estimates while also leveraging the high temporal frequency of PlanetScope data collection.

5 Capturing lake drainage over the melt season

Our improved ability to track lake depth and volumes using the combination of ICESat-2 and multi-sensor imagery can potentially provide new insights into patterns of lake drainage. Lake Julian (Fig. 7a) was selected for closer examination because on 15 May, both the airborne Operation IceBridge mission and ICESat-2 passed over this region, providing a unique stack of both airborne and satellite data. While we show only very high-resolution Operation Ice-Bridge CAMBOT imagery here, other instruments on board OIB could potentially provide valuable insight into the state of both surface hydrology and firn characteristics in future work. Additionally, there are cloud-free ICESat-2 RGT 727 passes over this lake both on 15 May and on 14 August 2019, providing a profile of the lake both when it was filled and after drainage. A second lake, Lake Niels (Fig. 7a), is examined briefly primarily to provide context. Although no altimetry
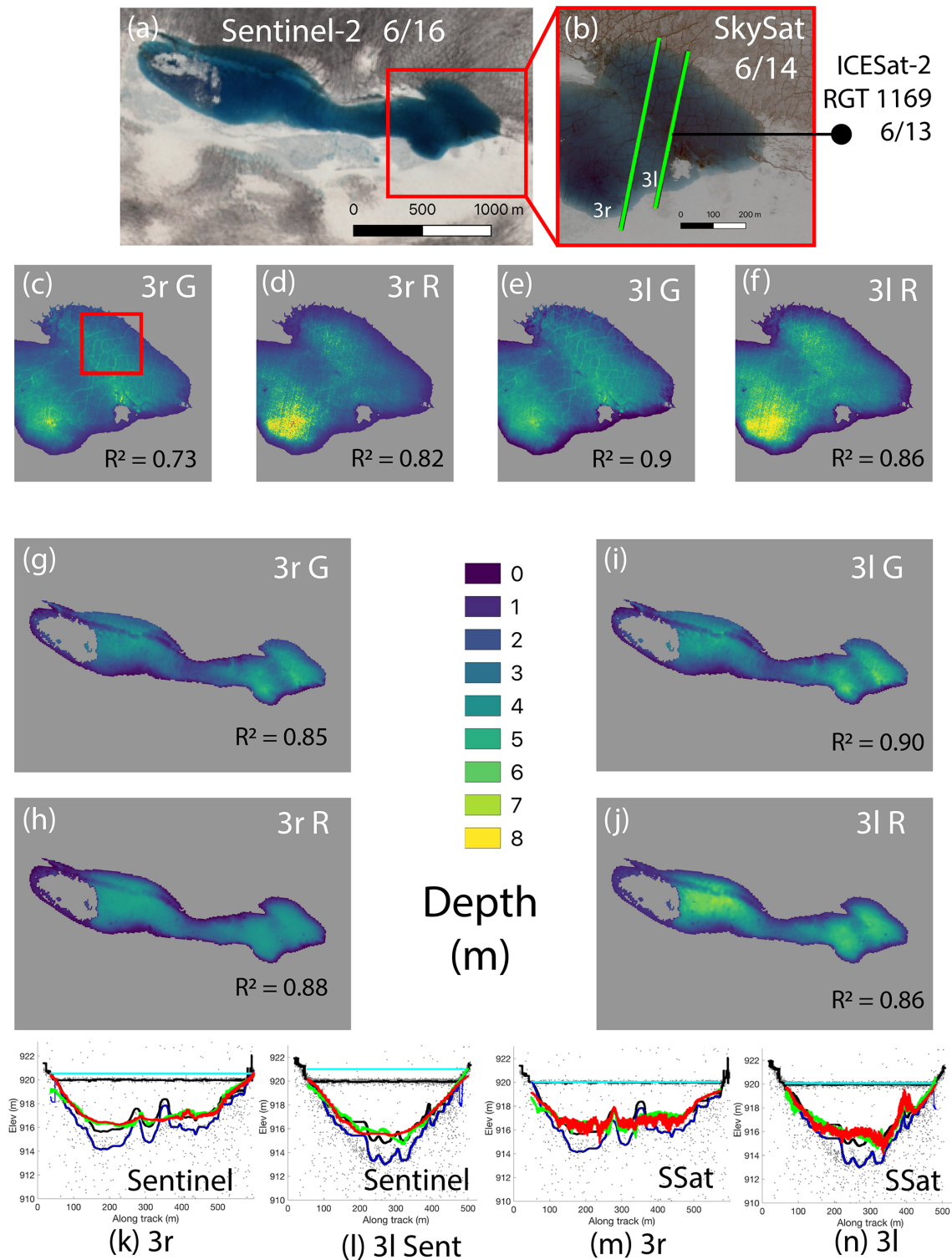
Figure 5. Watta-calculated and imagery-derived depths: Lake Cecily based on Sentinel-2 (**k, l**) and Planet SkySat (**m, n**); Lake Cecily false-color imagery from Sentinel-2 (**a**) and SkySat with ICESat-2 beam 3r and 3l (**b**); imagery-derived depths from Planet SkySat (**c–f**) and Sentinel-2 (**g–j**) with band–beam combination as shown. Estimates from the green band are indicated by "G", while those calculated from the red band are indicated by "R". The red box in (**c**) highlights region where underlying crevassing is captured.
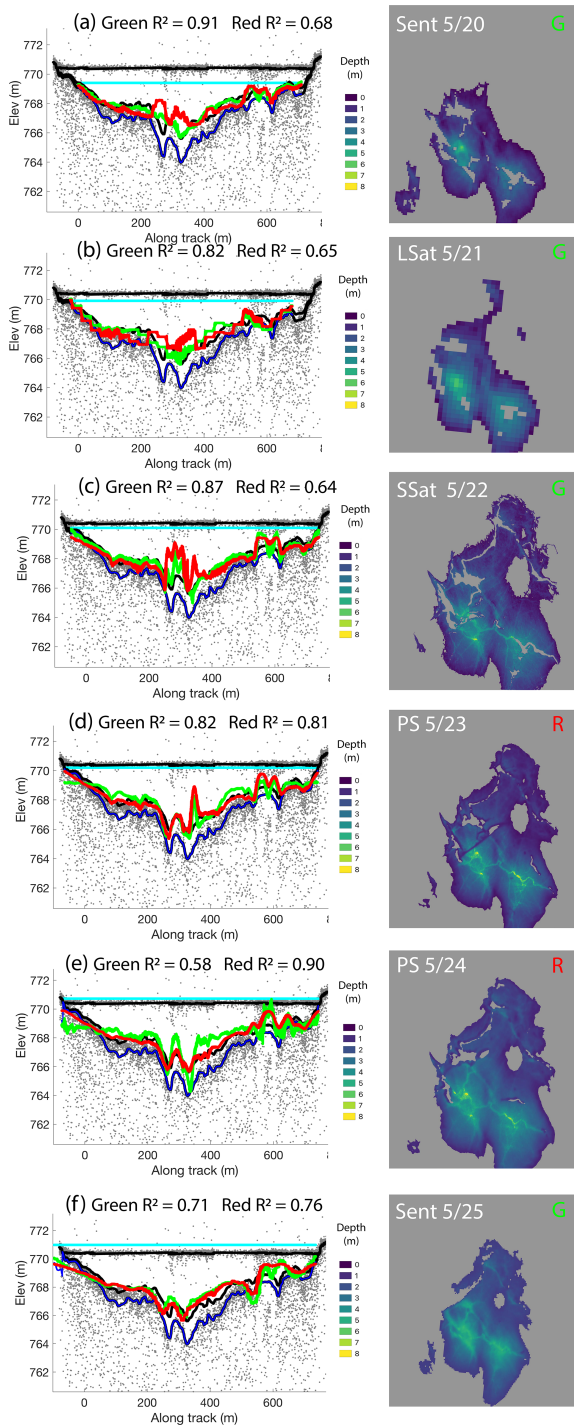
Figure 6. Lake Ayşe, filling over 5 d between 20 and 25 May with ICESat-2 pass on 23 May. Left column panels: profiles with Watta-calculated and imagery-derived depths from the green, indicated by "G", and red, indicated by "R", bands (with corresponding R^2 values inset; legend same as Fig. 4a). Right column panels: depth values derived from empirical estimate, with imagery source, date collected, and band used for depth estimate shown. Imagery source abbreviations are as follows: "LSat" for Landsat, "SSat" for Planet SkySat, "PS" for Planet PlanetScope, and "Sent" for Sentinel-2. Path of ICESat-2 spot over Lake Ayşe is shown in Fig. 1.

estimates are available over Lake Niels, imagery sources reveal a very different evolution and drainage pattern despite its being located only 3500 m from Lake Julian and consequently subject to many of the same atmospheric drivers. Within the larger region shown in Fig. 7a (see also Fig. S4), the percentage of the ice sheet surface covered in liquid water, as measured by the percentage of the region where NDWI ice values exceed 0.2, remains constant at around 3 % from May through June, with meltwater being spread more uniformly (less visibly collected in large hydrological features) over the ice sheet early in the season and shifting to larger lakes later in the season (Fig. S4). We note that this measure of melt extent does not translate directly to consistent meltwater volume; meltwater underneath the snow cover on Lake Niels was not estimated earlier in the season, while the deeper lakes which are present later in the season will contain larger water volumes.

Although elevation decreases overall toward the northwest, both lakes coincide with large-scale surface depressions calculated from the GIMP-2 DEM (Fig. 7), and this region experiences comparatively low ice velocities. Lake Niels is located in a deep surface depression, whereas the corresponding surface depression for Lake Julian is relatively shallow. Because both imagery and ICESat-2 are coregistered to the GIMP-2 DEM, we presume that all inaccuracies will be consistent (i.e., even if geolocation is incorrect in absolute terms, imagery and ICESat-2 should overlap).

5.1 Drainage mechanisms over Lake Julian from airborne and satellite-based imagery

The volume of Lake Julian begins to increase substantially on 9 May and reaches a maximum volume between 25 and 29 May (Fig. 8j–l). After 1 June, the lake begins to lose volume until only remnants are present on 10 June, which disappear almost entirely by 19 June (Fig. 8m–o). The surrounding region (i.e., a kilometer to the north and west) contain smaller bodies of water connected by streams. We note that while larger streams can be captured by Sentinel-2 imagery (Fig. 8j), many of the smaller streams present later in the season can only be reliably detected with imagery at a 1 m resolution or below (e.g., Figs. 8r and S5). The progression shown in Fig. 8 captures the development of an efficient drainage system over the season.

Three potential drainage mechanisms can be observed over Lake Julian. Firstly, we note a small stream ending in a spray of snow (alternatively, an ice bridge) which is potentially indicative of a moulin (Fig. 9b). However, an overflight of Operation IceBridge on 15 May (Fig. 9a) does not definitively show a moulin at the end of the incision, allowing for the possibility that the actual drainage occurred under the overlapping ice bridge. We also identify the point labeled B in Fig. 9a and b (also in Fig. 10d and e) as another potential drainage point. Presuming that drainage occurs at either location, lake volume could still increase slowly (as it does
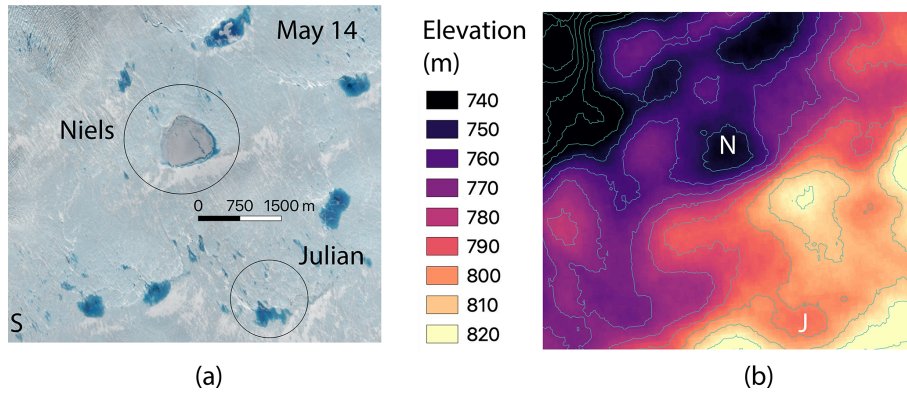
Figure 7. (a) Lake Niels and Lake Julian shown on 14 May 2019 using Sentinel-2 imagery as described in the "Data sources" section. **(b)** GIMP-2 DEM shown at same location with contours shown at 10 m intervals.
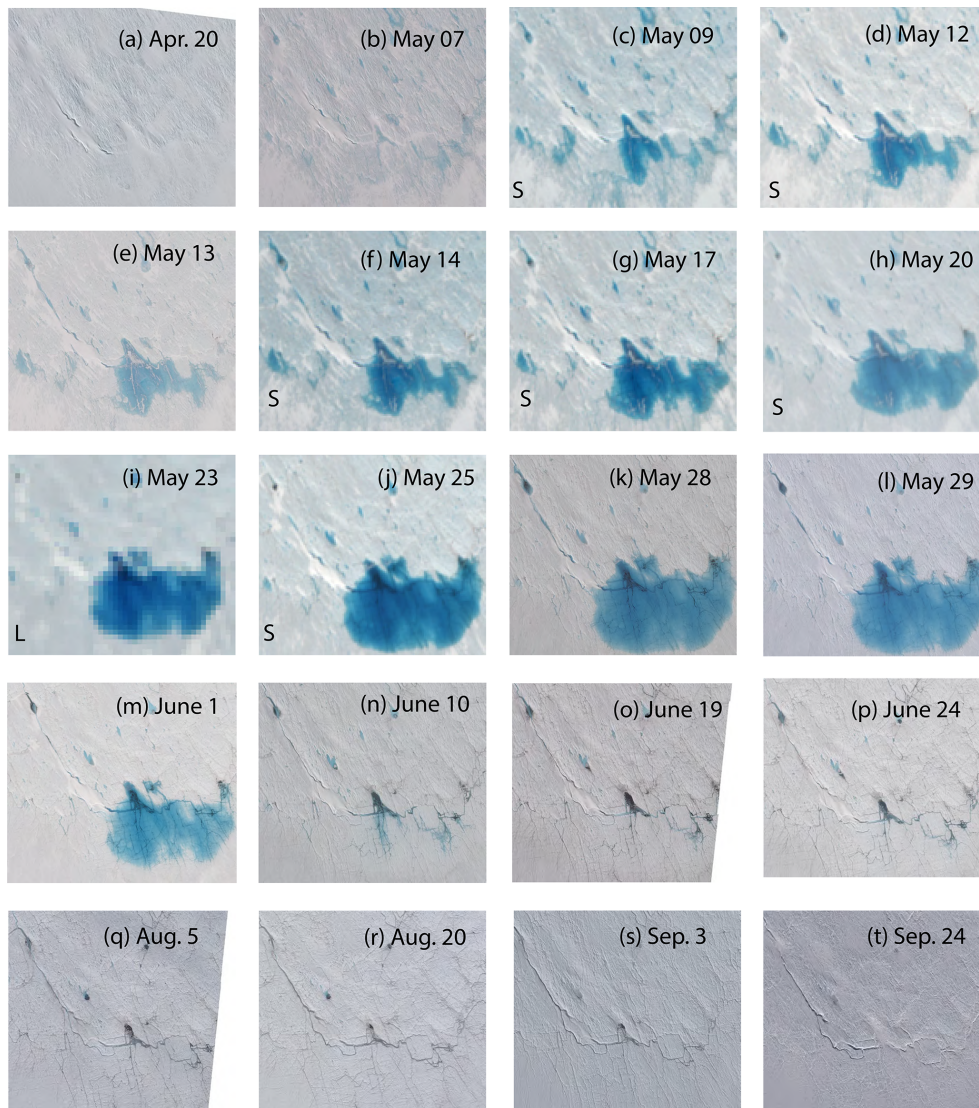
Figure 8. Imagery over Lake Julian shown from 20 April through 24 September 2019. All images use Planet SkySat Visual data unless otherwise indicated by letter on bottom left, with S indicating Sentinel and L indicating Landsat.

between 9 and 25 May) if the inflow rate exceeds the outflow rate of the lake. This dynamic is captured in a previous in situ study of lake drainage, which indicated that drainage through a moulin decelerated as the hydraulic head between the lake and the moulin declined (Tedesco et al., 2013).

However, following late May, SkySat imagery captures the development of a second stream directly south of the initial potential moulin (Fig. 9b). This small stream, which flows downstream (Fig. 7b), deepens throughout the season (Fig. 9c) with a very deep incision shown distinctly in imagery on 24 September (Fig. 8t). The development suggests that the relatively slow initial drainage from the potential moulin or point B accelerated due to increased drainage from a second small stream, draining Lake Julian almost entirely between 1 and 10 June (Fig. 8m–n). While smaller pre-existent streams to the right (Fig. 9b) may also have facilitated drainage, we assume that the newly incised stream to the left is the most likely cause for the rapid drainage due to the timing of its appearance. We note that smaller bodies of water are still apparent on the surface after the drainage of Lake Julian, some connected by very small stream networks which appear to be frozen-over by 24 September (Fig. 8t).
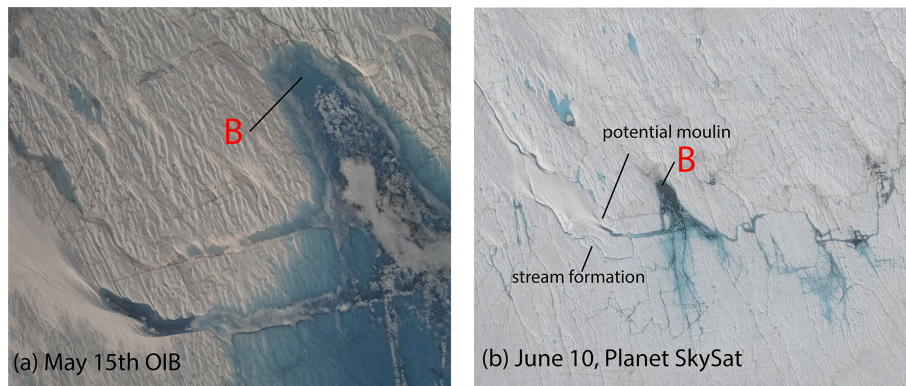
5.2 Drainage mechanisms over Lake Julian captured using Watta

Lake Julian reached a volume of $268\,120\,\mathrm{m}^3$ on 14 May, which was calculated using the green band from Sentinel-2 imagery on 14 May in conjunction with a Watta-based depth calculation from an ICESat-2 pass on 15 May (Fig. 10a and b). The time lag introduces uncertainty due to possible lake ablation. We assume that this uncertainty is not due to the discrepancy in dates (imagery having been captured on 14 May, whereas a deeper lake depth was captured by ICESat-2 on 15 May). This is because the methodology accounts for changing lake depths, presuming minimal lake ablation, matching Watta-calculated depth to the surface height where the edge of the lake is indicated by imagery (see Methods). The depth values calculated for 14 May indicate a relatively shallow lake (less than a maximum 4 m depth).

A comparison between the two passes of ICESat-2 RGT 727 (the second on 14 August) indicate uneven lowering in this region and potential slight ice motion, e.g., a small southward shift in the lowest point of the depth profile (point B) calculated on 15 May vs. on 14 August (Fig. 10c). We estimate large-scale surface lowering around $\sim 1\,\mathrm{m}$, based on the lowering calculated at higher elevations (Fig. 10c and d, where the x axis, showing the distance from an arbitrary start point, is greater than 800 m). By contrast, elevation changes where surface hydrology features exist show enhanced incision of a pre-existent stream/drainage point, as well as the development of a new stream (Fig. 10c and d, x-axis value between 0 and 200 m). The deepening of the lowest point in the lake could be the product of ice motion, but we assume that the elevation change of 2–3 m at this location

is the effect of lake ablation. This is due to the locations of ice layers being well-matched between imagery and Watta-calculated features (discussed shortly), suggesting that any ice motion was adjusted for in the geolocation step.

In addition to locations where Watta calculates a lake surface (Fig. 10d and e, label "B"), Watta also identifies regions where ice cover is probable. These are shown in cyan in Fig. 10d at locations A, C, and D and in imagery in Fig. 10e. Whereas lake surfaces are calculated at the horizontal resolution of the ICESat-2 ATL03 photon cloud, the ice surface class is assigned at a coarser resolution. This is because the Interpretive module assigns the "ice surface" class based on the presence of a flat surface under an overlying layer with more varied topography. While currently the algorithm potentially overestimates the extent of these regions, a first automatic pass can be used to identify larger regions where ice surfaces exist, after which manual inspection can then identify specific ice layers. Shown in Fig. 10d are lake B and three additional points where we identify ice layers using both Watta and manual inspection (A, C, D). Point B is also captured in Operation IceBridge CAMBOT imagery on 15 May (Fig. 9a). This is potentially a drainage point which retains meltwater as late as 14 August. This location is also covered by a floating ice layer on 14 May, suggesting that an ice layer had formed at the same place and settled at this point following drainage in the previous season. Point C corresponds to a deeply incised stream (which is not captured in the Watta profile calculated on 15 May), while point D corresponds to a smaller stream; both of these points were covered by Lake Julian during the last half of May. We note that the designation of point A is more ambiguous as it is collocated with an incision which was previously a stream but is weakly resolved in both Watta-based estimates and in the SkySat imagery collected on 20 August. The Watta designation of "ice surface" here is likely, but not unambiguous, as this method will capture both real ice surface and false dual returns as detailed in Sect. 3.1. The main attributes typical of the false dual returns are a strong top surface over surface water in a flat region, followed by weaker returns at predictable intervals ($\sim 0.45\,\mathrm{m}$ and possibly $\sim 0.90\,\mathrm{m}$ for the specular return, ~ 2.3 and $\sim 4.2\,\mathrm{m}$ for the instrument echo). In this case, a specular return would be the most likely cause for a false dual return due to the spacing. However, we first note that the surface in this region is not flat, and we do not see the predicted strong surface return followed by a weaker echo ("surface" and "ice" layers are of equal thickness). Additionally (a) in the case of point B, the top layer contains no dual return, and (b) in the case of C, a distinct gap occurs in the surface. Both of these correspond to ice/water in imagery. For point A and point D, imagery suggests that these points occur at a convergence of streams. These could, however, be either water or ice as no distinctive bottom return is detected. With the current available information, the "ice surface" detection will still require manual inspection; future

Figure 9. Mechanisms of lake drainage over Lake Julian. **(a)** CAMBOT imagery from Operation IceBridge flight on 15 May 2019 (30 cm resolution). **(b)** SkySat imagery ($\sim$ 1 m resolution) on 10 June after large-scale drainage.
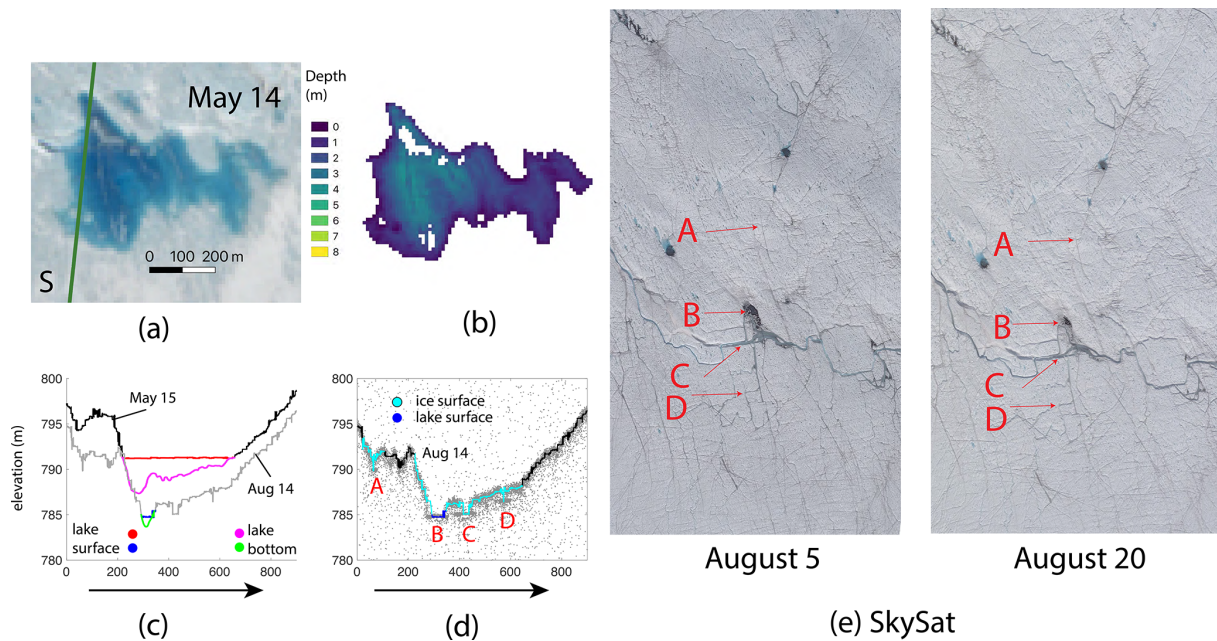

Figure 10. ICESat-2 RGT 727 over Lake Julian. **(a)** Sentinel-2-based imagery acquired on 14 May 2019 with ICESat-2 RGT 727 gt1l (occurring on 15 May and 14 August 2019) overlapping in green. Operation IceBridge overpass on 15 May 2019 is directly coincident with the ICESat-2 line. **(b)** Lake depth derived from Watta **(c)** and Sentinel-2 **(a)** imagery. **(c)** Watta calculated from ICESat-2 on 15 May and 14 August. **(d)** Watta-calculated surface features over photon cloud on 14 August. Points A–D discussed in text. **(e)** Points A–D shown over Planet SkySat imagery collected on 5 and 20 August.

improvements to the code may account for the known issue with false dual returns as knowledge in this area develops.

5.3 Lake Niels, partial drainage and refreeze

In comparison to Lake Julian, Lake Niels begins and ends the melt season as a frozen lake. By 9 May, the ice surface begins to melt, and the lake surface area expands substantially. However, by 13 May (Fig. 11d), imagery captures an insulating layer of snow, after which the lake expands until 26 June. By 20 July, slow lake drainage is evident via a stream which is identified in Fig. 11a and is first observed to contain a sub-

stantial quantity of liquid water on 19 June (Fig. 11h). We observe that the stream is clearly incised both on 20 April (Fig. 11b) and on 24 September (Fig. 11m), when the lake is likely frozen over, based on imagery. In comparison to Lake Julian, which was located in a relatively shallow depression, Lake Niels is located in a deep depression (Fig. 7), and neither drains early in the season nor connects to an efficient drainage system. Although these lakes are subject to similar atmospheric drivers, the differences in drainage patterns highlight how local topography and the corresponding depth of lakes can influence how meltwater is either retained on
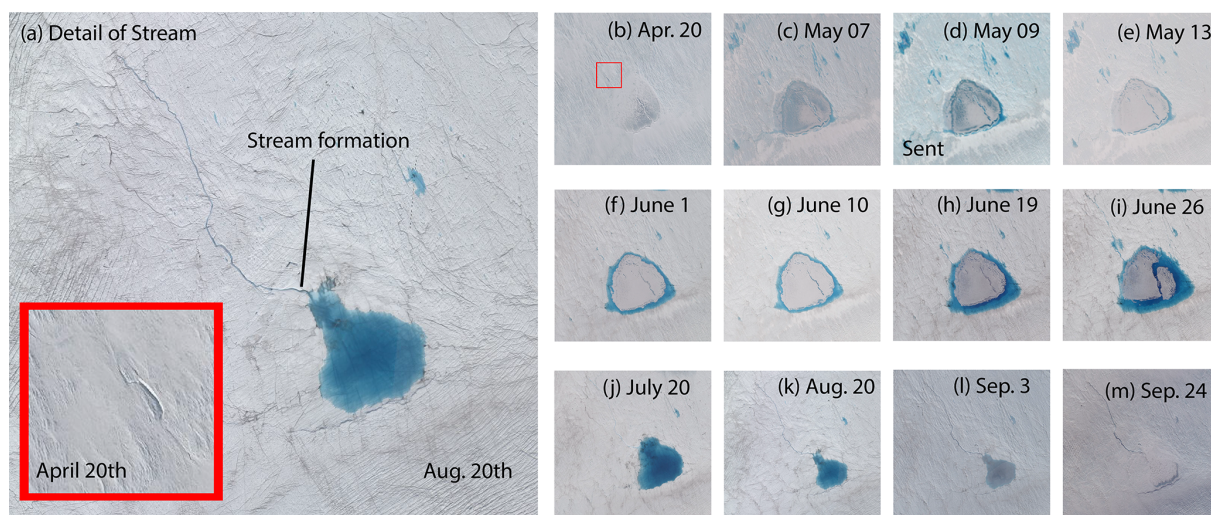
Figure 11. Lake Niels shown between 20 April and 4 September 2019. Panel **(a)** shows stream detail from 20 August (main panel) with stream detail on 20 April (inset, with region indicated in panel **b**). All imagery is from Planet SkySat Visual imagery except on 9 May (when Sentinel-2 imagery is used, indicated with "Sent").

the ice sheet or drained downstream or into englacial or subglacial pathways. We note that surface topography, in turn, is strongly influenced by basal topography, thus linking total runoff to surface expression of bed topography (Ignéczi et al., 2018).

6 Conclusions

This study represents initial work developing the Watta algorithm for lake depth estimates, as well as subsurface ice detection, using a unique stacked dataset over western Greenland during the intense 2019 melt season. We demonstrate the potential of ICESat-2 for automated lake detection and depth estimation, as well as how empirically derived depths derived from a combination of imagery sources can complement each source's strengths and weaknesses. For example, while Landsat is only available at a low resolution, it provides a rich historical record, as well as high geolocational accuracy (at 5 m), which is leveraged here to better geolocate imagery from Planet Labs. Similarly, while PlanetScope data contain several known issues with radiometry and geolocation, imagery is available at a high spatial and temporal resolution. As demonstrated in our test cases, a time series constructed from multiple sources can provide valuable information about the evolution of ice cover and drainage mechanisms in addition to volume estimates. Given the accelerating sophistication of altimetry-based observations, ongoing efforts to improve geolocation, radiometric quality, or temporal frequency of high-resolution imagery are crucial. Additionally, the availability of simultaneous imagery and altimetry would enhance the capabilities of other satellite imagery

sources to fill out the time series by providing a calibration standard.

While this initial study focused on lakes in grounded ice in Greenland, Watta can potentially be applied to Antarctic melt lakes as well. Additionally, lake depths calculated empirically can potentially be used to calibrate physically based methods towards developing ice-sheet-wide time series for the evolution of surface hydrology.

Our algorithm successfully detects a wide variety of lake types automatically and can be applied to the growing set of ICESat-2 and imagery data over large sections of Antarctica and Greenland. Identification of narrow stream features on sloping surfaces, however, still needs visual verification due to a large number of false positives. This will be addressed in future work, together with adding features to the interpretive layer, including slush layers as well as cracks, using the Planet SkySat imagery dataset for testing purposes. In addition to these improvements, Watta, which is currently written in MATLAB, is available in GitHub with documentation but will eventually be moved to an open-source language.

Code availability. Code for Watta can be found here: https://doi.org/10.5281/zenodo.5655860 (Datta and Wouters, 2021).

Imagery, IDs for which can be found in the Supplement, can be accessed at the following urls:

- for Planet imagery: https://www.planet.com/ (Planet Labs, 2020);
- for Sentinel-2 and Landsat 7 and 8 imagery: https:// earthexplorer.usgs.gov/ (USGS, 2021);
- for ICESat-2 ATL03: https://doi.org/10.5067/ATLAS/ATL03.003 (Neumann et al., 2021).

References

Albright, A. and Glennie, C.: Nearshore Bathymetry From Fusion of Sentinel-2 and ICESat-2 Observations, IEEE Geosci. Remote Sens. Lett., 18, 900–904, https://doi.org/10.1109/LGRS.2020.2987778, 2020.

Arthur, J. F., Stokes, C. R., Jamieson, S. S. R., Carr, J. R., and Leeson, A. A.: Distribution and seasonal evolution of supraglacial lakes on Shackleton Ice Shelf, East Antarctica, The Cryosphere, 14, 4103–4120, https://doi.org/10.5194/tc-14-4103-2020, 2020.

Banwell, A. F., Caballero, M, Arnold, N., Blasser, N., Mac Cathles, L., and MacAyeal, D.: Supraglacial lakes on the Larsen B ice shelf, Antarctica, and at Paakitsoq, West Greenland: a comparative study, Ann. Glaciol., 55, 1–8, https://doi.org/10.3189/2014AoG66A049, 2014.

Bell, R. E., Banwell, A. F., Trusel, L. D., and Kingslake, J.: Antarctic surface hydrology and impacts on ice-sheet mass balance, Nat. Clim. Change, 8, 1044–1052, https://doi.org/10.1038/s41558-018-0326-3, 2018.

Besl, P. J. and McKay, N. D.: A method for registration of 3-D shapes, IEEE T. Pattern Anal. Mach. Intel., 14, 239–256, https://doi.org/10.1109/34.121791, 1992.

Box, J. and Ski, K.: Remote sounding of Greenland supraglacial melt lakes: Implications for subglacial hydraulics, J. Glaciol., 53, 257–265, https://doi.org/10.3189/172756507782202883, 2007.

Bradley, D. and Roth, G.: Adaptive Thresholding using the Integral Image, J. Graph. Tool., 12, 13–21, https://doi.org/10.1080/2151237X.2007.10129236, 2007.

Datta, R. and Wouters, B.: Source code for the Watta algorithm, version 1, Zenodo [code], https://doi.org/10.5281/zenodo.5655860, 2021.

Dell, R., Arnold, N., Willis, I., Banwell, A., Williamson, A., Pritchard, H., and Orr, A.:Lateral meltwater transfer across an Antarctic ice shelf, The Cryosphere, 14, 2313–2330, https://doi.org/10.5194/tc-14-2313-2020, 2020.

Fair, Z., Flanner, M., Brunt, K. M., Fricker, H. A., and Gardner, A.: Using ICESat-2 and Operation IceBridge altimetry for supraglacial lake depth retrievals, The Cryosphere, 14, 4253–4263, https://doi.org/10.5194/tc-14-4253-2020, 2020.

Fricker, H. A., Arndt, P., Brunt, K. M., Datta, R. T., Fair, Z., Jasinski, M. F., Kingslake, J., Magruder, L. A., Moussavi, M., Pope, A., Spergel, J. J., Stoll, J. D., and Wouters, B.: ICESat-2 melt depth retrievals: Application to surface melt on Amery Ice Shelf, East Antarctica, Geophys. Res. Lett., 48, e2020GL090550, https://doi.org/10.1029/2020GL090550, 2020.

Gledhill, L. A. and Williamson, A. G.: Inland advance of supraglacial lakes in north-west Greenland under recent climatic warming, Ann. Glaciol., 59, 66–82, https://doi.org/10.1017/aog.2017.31, 2018.

Howat, I. M., de la Peña, S., van Angelen, J. H., Lenaerts, J. T. M., and van den Broeke, M. R.: Brief Communication:Expansion of meltwater lakes on the Greenland Ice Sheet, The Cryosphere, 7, 201–204, https://doi.org/10.5194/tc-7-201-2013, 2013.

Howat, I. M., Negrete, A., and Smith, B. E.: The Greenland Ice Mapping Project (GIMP) land classification and surface elevation data sets, The Cryosphere, 8, 1509–1518, https://doi.org/10.5194/tc-8-1509-2014, 2014.

Ignéczi, Á., Sole, A. J., Livingstone, S. J., Ng, F. S. L., and Yang, K.: Greenland Ice Sheet Surface Topography and Drainage Structure Controlled by the Transfer of Basal Variability, Front. Earth Sci., 6, 101, https://doi.org/10.3389/feart.2018.00101, 2018.

IPCC: IPCC Special Report on the Ocean and Cryosphere in a Changing Climate, edited by: Pörtner, H.-O., Roberts, D. C., Masson-Delmotte, V., Zhai, P., Tignor, M., Poloczanska, E., Mintenbeck, K., Alegría, A., Nicolai, M., Okem, A., Petzold, J., Rama, B., and Weyer, N. M., available at: https://www.ipcc.ch/srocc/cite-report/ (last access: 10 November 2021), 2019.

Lai, C.-Y., Kingslake, J., Wearing, M. G., Chen, P.-H. C., Gentine, P., Li, H., Spergel, J. J., and van Wessem, J. M.: Vulnerability of Antarctica's ice shelves to meltwater-driven fracture, Nature, 584, 574–578, https://doi.org/10.1038/s41586-020-2627-8, 2020.

Leeson, A. A., Shepherd, A., Briggs, K., Howat, I., Fettweis, X., Morlighem, M., and Rignot, E.: Supraglacial lakes on the Greenland ice sheet advance inland under warming climate, Nat. Clim. Change, 5, 51–55, https://doi.org/10.1038/nclimate2463, 2015.

Legleiter, C. J., Tedesco, M., Smith, L. C., Behar, A. E., and Overstreet, B. T.: Mapping the bathymetry of supraglacial lakes and streams on the Greenland ice sheet using field measurements and high-resolution satellite images, The Cryosphere, 8, 215–228, https://doi.org/10.5194/tc-8-215-2014, 2014.

Lu, X., Hu, Y., Yang, Y., Vaughan, M., Palm, S., Trepte, C., Omar, A., Lucker, P., and Baize, R.: Enabling value added scientific applications of ICESat-2 data with effective removal of afterpulses, Earth Space Sci., 8, e2021EA001729, https://doi.org/10.1029/2021EA001729, 2021.

MacFerrin, M., Machguth, H., van As, D., Charalampidis, C., Stevens, C. M., Heilig, A., Vandecrux, B., Langen, P. L., Mottram, R., Fettweis, X., van den Broeke, M. R., Pfeffer, W. T., Moussavi, M. S., and Abdalati, W.: Rapid expansion of Greenland's low- permeability ice slabs, Nature, 573, 403–407, https://doi.org/10.1038/s41586-019-1550-3, 2019.

Magruder, L. A., Brunt, K. M., Neumann, T., Klotz, B., and Alonzo, M: Passive ground-based optical techniques for monitoring the on-orbit ICESat-2 altimeter geolocation and footprint diameter, Earth Space Sci., 8, e2020EA001414, https://doi.org/10.1002/essoar.10504571.1, 2021.

Martino, A., Field, C. T., and Ramos-Izquierdo, L.: ICESat-2/ATLAS Instrument Linear System Impulse Response, Earth Space Sci., https://doi.org/10.1002/essoar.10504651.1, in review, 2020.

Mouginot, J., Rignot, E., Bjørk, A. A., van den Broeke, M., Millan, R., Morlighem, M., Noël, B., Scheuchl, B., and Wood, M.: Forty- six years of Greenland Ice Sheet mass balance from 1972 to 2018, P. Natl. Acad. Sci. USA, 116, 9239, https://doi.org/10.1073/pnas.1904242116, 2019.

Moussavi, M., Pope, A., Halberstadt, A. R. W., Trusel, L. D., Cioffi, L., and Abdalati, W.: Antarctic Supraglacial Lake Detection Using Landsat 8 and Sentinel-2 Imagery: Towards Continental Generation of Lake Volumes, Remote Sens., 12, 134, https://doi.org/10.3390/rs12010134, 2020.

Moussavi, M. S., Abdalati, W., Pope, A., Scambos, T., Tedesco, M., MacFerrin, M., and Grigsby, S.: Derivation and validation of supraglacial lake volumes on the Greenland Ice Sheet from high-resolution satellite imagery, Remote Sens. Environ., 183, 294–303, https://doi.org/10.1016/j.rse.2016.05.024, 2016.

Neumann, T. A., Martino, A. J., Markus, T., Bae, S., Bock, M. R., Brenner, A. C., Brunt, K. M., Cavanaugh, J., Fernandes, S. T., Hancock, D. W., Harbeck, K., Lee, J., Kurtz, N. T., Luers, P. J., Luthcke, S. B., Magruder, L., Pennington, T. A., Ramos-Izquierdo, L., Rebold, T., Skoog, J., and Thomas, T. C.: The Ice, Cloud, and Land Elevation Satellite – 2 mission: A global geolocated photon product derived from the Advanced Topographic Laser Altimeter System, Remote Sens. Environ., 233, 111325, https://doi.org/10.1016/j.rse.2019.111325, 2019.

Neumann, T. A., Brenner, A., Hancock, D., Robbins, J., Saba, J., Harbeck, K., Gibbons, A., Lee, J., Luthcke, S. B., Rebold, T., et al.: ATLAS/ICESat-2 L2A Global Geolocated Photon Data, Version 4 [Indicate subset used], NASA National Snow and Ice Data Center Distributed Active Archive Center [data set], Boulder, Colorado, USA, https://doi.org/10.5067/ATLAS/ATL03.003, 2021.

Parrish, C. E., Magruder, L. A., Neuenschwander, A. L., Forfinski-Sarkozi, N., Alonzo, M., and Jasinski, M.: Validation of ICESat-2 ATLAS Bathymetry and Analysis of ATLAS's Bathymetric Mapping Performance, Remote Sens., 11, 1634, https://doi.org/10.3390/rs11141634, 2019.

Planet Labs: Daily Earth Data to See Change and Make Better Decisions, available at: https://www.planet.com, last access: 15 September 2020.

Pope, A., Scambos, T. A., Moussavi, M., Tedesco, M., Willis, M., Shean, D., and Grigsby, S.: Estimating supraglacial lake depth in West Greenland using Landsat 8 and comparison with other multispectral methods, The Cryosphere, 10, 15–27, https://doi.org/10.5194/tc-10-15-2016, 2016.

Rignot, E., Mouginot, J., Scheuchl, B., van den Broeke, M., van Wessem, M. J., and Morlighem, M.: Four decades of Antarctic Ice Sheet mass balance from 1979–2017, P. Natl. Acad. Sci. USA, 116, 1095–1103, https://doi.org/10.1073/pnas.1812883116, 2019.

Sasgen, I., Wouters, B., Gardner, A. S., King, M. D., Tedesco, M., Landerer, F. W., Dahle, C., Save, H., and Fettweis, X.: Return to rapid ice loss in Greenland and record loss in 2019 detected by the GRACE-FO satellites, Commun. Earth Environ., 1, 8, https://doi.org/10.1038/s43247-020-0010-1, 2020.

Saunier, S,: TN on Quality Assessment for PlanetScope (DOVE), available at: https://earth.esa.int/eogateway/documents/20142/1305226/EDAP-REP-007-TN-on-Quality-Assessment-for-PlanetScope-,DOVE-v1.2.pdf (last access: 5 November 2021), 2020.

Scheffler, D., Hollstein, A., Diedrich, H., Segl, K., and Hostert, P.: An Automated and Robust Open-Source Image Co-Registration Software for Multi-Sensor Satellite Data, Remote Sens., 9,676, https://doi.org/10.3390/rs9070676, 2017.

Schlegel, N.-J., Seroussi, H., Schodlok, M. P., Larour, E. Y., Boening, C., Limonadi, D., Watkins, M. M., Morlighem, M., and van den Broeke, M. R.: Exploration of Antarctic Ice Sheet 100-year contribution to sea level rise and associated model uncertainties using the ISSM framework, The Cryosphere, 12, 3511–3534, https://doi.org/10.5194/tc-12-3511-2018, 2018.

Slater, T., Hogg, A. E., and Mottram, R.: Ice-sheet losses track high-end sea-level rise projections, Nat. Clim. Change, 10, 879–881, https://doi.org/10.1038/s41558-020-0893-y, 2020.

Smith, B., Fricker, H. A., Holschuh, N., Gardner, A. S., Adusumilli, S., Brunt, K. M., Csatho, B., Harbeck, K., Huth, A., Neumann, T., Nilsson, J., and Siegfried, M. R.: Land ice height-retrieval algorithm for NASA's ICESat-2 photon-counting laser altimeter, Remote Sens. Environ., 233, 111352, https://doi.org/10.1016/j.rse.2019.111352, 2019.

Sneed, W. and Hamilton, G.: Validation of a method for determining the depth of glacial melt ponds using satellite imagery, Ann. Glaciol., 52, 15–22, https://doi.org/10.3189/172756411799096240, 2011.

Sneed, W. A. and Hamilton, G. S.: Evolution of melt pond volume on the surface of the Greenland Ice Sheet, Geophys. Res. Lett., 34, 15–22, https://doi.org/10.1029/2006GL028697, 2007.

Stokes, C. R., Sanderson, J. E., Miles, B. W. J., Jamieson, S. S. R., and Leeson, A. A.: Widespread distribution of supraglacial lakes around the margin of the East Antarctic Ice Sheet, Scient. Rep., 9, 13823, https://doi.org/10.1038/s41598-019-50343-5, 2019.

Tedesco, M. and Fettweis, X.: Unprecedented atmospheric conditions (1948–2019) drive the 2019 exceptional melting season over the Greenland ice sheet, The Cryosphere, 14, 1209–1223, https://doi.org/10.5194/tc-14-1209-2020, 2020.

Tedesco, M., Lüthje, M., Steffen, K., Steiner, N., Fettweis, X., Willis, I., Bayou, N., and Banwell, A.: Measurement and modeling of ablation of the bottom of supraglacial lakes in western Greenland, Geophys. Res. Lett., 39, L02502, https://doi.org/10.1029/2011GL049882, 2012.

Tedesco, M., Willis, I. C., Hoffman, M. J., Banwell, A. F., Alexander, P., and Arnold, N. S.: Ice dynamic response to two modes of surface lake drainage on the Greenland ice sheet, Environ. Res. Lett., 8, 034007, https://doi.org/10.1088/1748-9326/8/3/034007, 2013.

Thomas, N., Pertiwi, A. P., Traganos, D., Lagomasino, D., Poursanidis, D., Moreno, S., and Fatoyinbo, L.: Space-Borne Cloud-Native Satellite-Derived Bathymetry (SDB) Models Using ICESat-2 And Sentinel-2, Geophys. Res. Lett., 48, e2020GL092170, https://doi.org/10.1029/2020GL092170, 2021.

Trusel, L. D., Das, S. B., Osman, M. B., Evans, M. J., Smith, B. E., Fettweis, X., McConnell, J. R., Noël, B. P. Y., and van den Broeke, M. R.: Nonlinear rise in Greenland runoff in response to post-industrial Arctic warming, Nature, 564, 104–108, https://doi.org/10.1038/s41586-018-0752-4, 2018.

USGS: Earth Explorer, available at: https://earthexplorer.usgs.gov, last access: 15 January 2021.

van den Broeke, M. R., Enderlin, E. M., Howat, I. M., Kuipers Munneke, P., Noël, B. P. Y., van de Berg, W. J., van Meijgaard, E., and Wouters, B.: On the recent contribution of the Greenland ice sheet to sea level change, The Cryosphere, 10, 1933–1946, https://doi.org/10.5194/tc-10-1933-2016, 2016.

Williamson, A. G., Banwell, A. F., Willis, I. C., and Arnold, N. S.: Dual-satellite (Sentinel-2 and Landsat 8) remote sensing of supraglacial lakes in Greenland, The Cryosphere, 12, 3045–3065, https://doi.org/10.5194/tc-12-3045-2018, 2018.

Yang, K. and Smith, L. C.: Supraglacial Streams on the Greenland Ice Sheet Delineated From Combined Spectral–Shape Information in High-Resolution Satellite Imagery, IEEE Geosci. Remote Sens. Lett., 10, 801–805, https://doi.org/10.1109/LGRS.2012.2224316, 2013.

Yang, K., Smith, L. C., Sole, A., Livingstone, S. J., Cheng, X., Chen, Z., and Li, M.: Automated High-Resolution Satellite Image Registration Using Supraglacial Rivers on the Greenland Ice Sheet, IEEE J. Select. Top. Appl. Earth Obs. Remote Sens., 10, 845–856, https://doi.org/10.1109/JSTARS.2016.2617822, 2017.